ACS APPLIED MATERIALS & INTERFACES

www.acsami.org

Forum Article

Exploration of the Underlying Space in Microscopic Images via Deep Learning for Additively Manufactured Piezoceramics

Wenhua Yang, Zhuo Wang, Tiannan Yang, Li He, Xuan Song, Yucheng Liu,* and Lei Chen*

Cite This: *ACS Appl. Mater. Interfaces* 2021, 13, 53439–53453

Read Online

ACCESS | Metrics & More | Article Recommendations | Supporting Information

ABSTRACT: There has been a surge of interest in applying deep learning (DL) to microstructure generation and materials design. However, existing DL-based methods are generally limited in generating (1) microstructures with high resolution, (2) microstructures with high variability, (3) microstructures with guaranteed periodicity, and (4) highly controllable microstructures. In this study, a DL approach based on a stacked generative adversarial network (StackGAN-v2) is proposed to overcome these shortcomings. The presented modeling approach can reconstruct high-fidelity microstructures of additively manufactured piezoceramics with different resolutions, which are statistically equivalent to original microstructures either experimentally observed or numerically predicted. Advantages of the proposed modeling approach are also illustrated in terms of its capability in controlling the probability density function (PDF) of grain size, grain orientation, and micropore in a large space, which would have significant benefits in exploring the effects of these microstructure features on the piezoelectricity of piezoceramics. In the meantime, periodicity of the microstructures has been successfully introduced in the developed model, which can critically reduce the simulation volume to be considered as a representative volume element (RVE) during computational calculation of piezoelectric properties. Therefore, this DL approach can significantly accelerate the process of designing optimal microstructures when integrating with computational methods (e.g., fast Fourier spectral iterative perturbation (FSIPM)) to achieve desired piezoelectric properties. The proposed DL-based method is generally applicable to optimal design of a variety of periodic microstructures, allowing for maximum explorations of design spaces and fine manipulations of microstructural features.

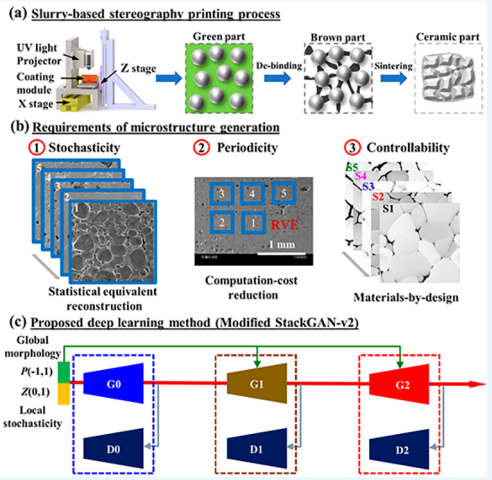

KEYWORDS: *micromorphology control, periodic microstructure, statistical reconstruction, high-resolution microstructure, deep learning, piezoelectricity, additive manufacturing*

1. INTRODUCTION

Piezoceramics such as lead zirconate titanate (PZT) and barium titanate ($BaTiO_3$, BTO) have received both academic and industrial interests because they can be used in tremendous applications, for instance, sensors, actuators, and energy harvesting devices.[1] The performances of these applications critically depend on their properties, i.e., piezoelectric coefficients.[2] These coefficients in turn significantly rely on the characteristics of the microstructure features of those piezoceramics.[3,4] On the other hand, ceramics fabricated by various manufacturing processes contain different kinds of microstructure features, such as grains and residual micropores of different sizes, shapes, and spatial distributions. In particular, the piezoceramics fabricated by additive manufacturing (AM) processes exhibit more complex microstructure features than those produced by conventional approaches.[5,6] For instance, higher volume fraction (VF) of microporosity[4] along the grain boundaries (GBs) (see Figure 1b, c) are usually observed in the AM-produced piezoceramics because more organic binder is contained in the feedstock, which will be burned out in the following debinding and sintering processes as depicted in Figure 1a. It has been well recognized that the VF, size, shape, orientation, and spatial distribution of grains and micropores all have significant effects on the piezoelectric properties of piezoceramics[7] and thus the energy harvesting performance and other related applications.[8,9] For instance, Chen et al.[7] indicated a 0.1 VF of micropores causes about a 50% decrease in the piezoelectric constant d_{33} in $(1-x)Pb(Mg_{1/3}Nb_{2/3})$-$O_{3-x}PbTiO_3$ (PMN−PT) ceramics. Meanwhile, in perfectly textured PMN−PT ceramics, the d_{33} could be almost 8 times larger than that with random crystal orientation. Nan et al.[10]

Special Issue: Artificial Intelligence/Machine Learning for Design and Development of Applied Materials

Received: July 8, 2021
Accepted: August 23, 2021
Published: September 1, 2021

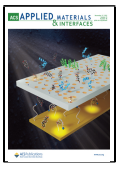

https://doi.org/10.1021/acsami.1c12945
ACS Appl. Mater. Interfaces 2021, 13, 53439–53453

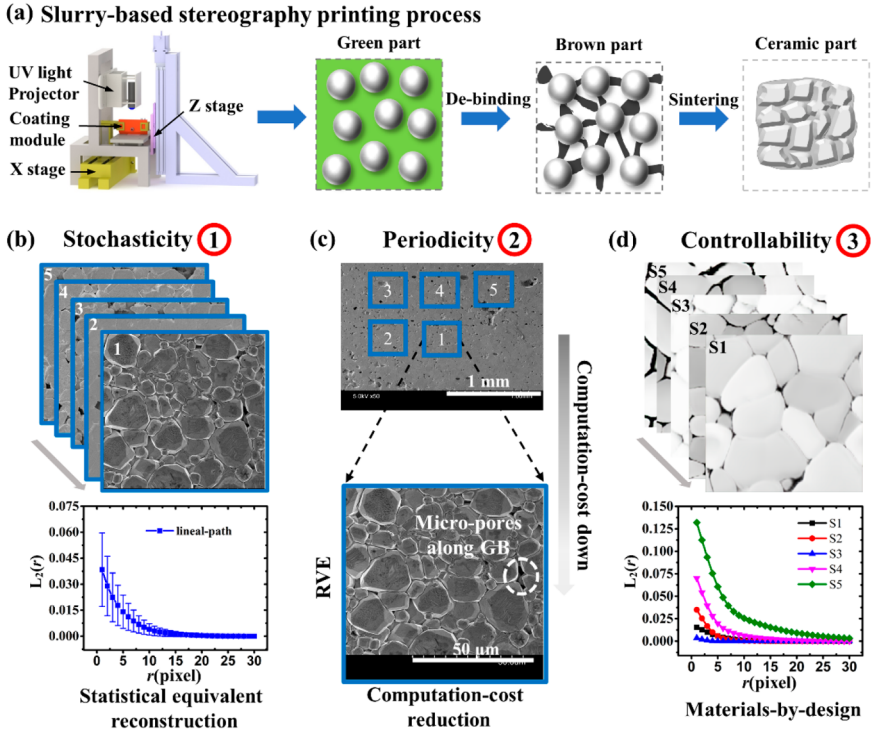

Figure 1. (a) Schematic of slurry-based stereography printing process for manufacturing piezoceramics. Motivations of the present study: (b) to reconstruct statistically equivalent microstructures based on the stochasticity of microstructures, (c) to generate microstructures with periodic boundaries to reduce computational cost, and (d) to provide a pathway to materials-by-design through high controllability of micromorphologies in a large space. The graphs in b and d are plotted with the lineal-path functions $L_2(r)$ of the micropore phase. Specifically, the graph in b plots the average of lineal-path functions of the five microstructures, whereas the curves in d are for each corresponding microstructure.

stated that a decreasing aspect ratio of grain may enhance the d_{33} of BTO ceramics. Zheng et al.[11] found both relative permittivity κ_{33} and d_{33} of poled BTO ceramics increase enormously with the decrease in average grain size at room temperature.

Computational methods, including the finite element method (FEM) and the fast Fourier transform (FFT) based method, have been applied to quantitatively analyze the microstructure effects on the effective piezoelectric properties of piezoceramics or piezocomposites. Microstructures are stochastic in nature (see Figure 1b); the statistical functions[12] (e.g., $L_2(r)$ lineal-path function) of micropores and the probability density functions (PDFs) of grain sizes, orientations, etc., have significant effects[13,14] on the piezoelectric properties of piezoceramics. For example, the micropores whose distribution aligns in the poling direction can enhance piezoelectric sensitivity,[15] whereas the micropores that locate at the grain boundaries can decrease the d_{33} more than those within grains.[7] Hence, to acquire statistically structure−property relations[7] from the calculations using the aforementioned computational methods, a large ensemble of such calculations using a large quantity of statistically representative microstructures is strongly required, which necessitates a method to generate an ensemble of microstructures that are statistically equivalent to the experimentally observed microstructures. In addition, the calculation of effective piezoelectric properties using the computational methods is usually very computationally costly, and thus RVE such as microstructures with periodic boundaries are critically desired to ensure high computational efficiency yet with relatively high accuracy (see Figure 1c). On the other hand, from a material-by-design aspect, high-throughput computational simulations are needed to guide the design of microstructures to achieve the desirable piezoelectric properties, which require a high controllability to generate the microstructure morphologies in a large design space (see Figure 1d).

Conventional approaches to reconstruct statistically equivalent microstructures include statistical function-based[16,17] and physical descriptor-based numerical modeling methods.[4,18] Statistical function-based approaches employ correlation functions and/or lineal-path functions to characterize and reconstruct microstructures. Although they are widely used, potential information loss (e.g., dispersive characteristic) often occurs in the dimension reduction process required to represent high-dimensional microstructures. For instance, using principal component analysis (PCA) to remove insignificant dimensions would induce information loss, when conducting a transformation of microstructure representation. Computational intractability is another disadvantage of the statistical function-based methods, especially in the case of the high-order correlation functions (e.g., three-point correlation functions and above). Moreover, tedious optimization (e.g., simulated annealing) for microstructure reconstructions is needed,[19] which make it extremely difficult and computationally inefficient to generate large quantities of microstructures with distinct microstructure features. There are many physical descriptor-based models to generate grain microstructures, many of which were developed to simulate grain growth, such as the Potts model,[20,21] the phase-field grain growth model (PFM), the front tracking model,[22,23] Voronoi tessellation,[24] and the vertex model.[25] Among these models, the Potts and PFM are the most robust and versatile and certainly the most

https://doi.org/10.1021/acsami.1c12945
ACS Appl. Mater. Interfaces 2021, 13, 53439−53453

highly developed and widely applied.[26−28] However, these approaches usually require identifying the characteristics of microstructure features and compare the PDFs of those characteristics between real and synthetic microstructures; thus, it is still difficult and time-consuming to reconstruct statistically equivalent microstructures.[4]

Deep learning (DL) based methods could be a promising alternative to tackle the shortcomings of the conventional approaches. In particular, the DL methods have no information loss because dispersive approximations are not required. Instead, the DL methods generate microstructures using specially designed deep convolutional neural networks,[29,30] which feature large model capacity and generalities, to achieve a low-dimensional and nonlinear embedding of high-dimensional microstructures. In addition, the DL methods are model-based and can promptly generate large quantities of microstructures by inputting different values of their intrinsic parameters.[31,32] Thus, under these circumstances, many DL techniques have been successfully applied to microstructure characterizations and reconstructions.[33−35] Cang et al.[36] employed a convolutional deep belief network (CDBN) to hierarchically extract microstructure representations and realize reconstructions for the chosen multiscale anisotropic alloy microstructure. But their model relies on a heuristic postprocessing step which is specifically designed for the alloy system studied. Li et al.[35] proposed a transfer learning approach to reconstruct microstructures. However, the optimization objective is achieved by minimizing the style differences (defined by a Gram matrix) between synthetic and real microstructures. Hence, the characteristics of microstructure features can be spanned only in the vicinity of real samples.

Another DL-based method, the generative adversarial networks (GAN),[37] and its derivatives[38−40] have been widely adopted in materials science[41−43] in recent years. Ma et al.[41] employed pix2pix[39] based on conditional generative adversarial networks (CGAN)[38] to generate synthetic images with the styles of selected microscopic images. However, the output from their network was not highly stochastic even after noise vectors had been introduced in the generator. This minor stochasticity in the generated images presents a crucial limitation in generating large quantities of microstructures that can span the space of desired microstructure features. Chun et al.[42] proposed to use patch-based GAN to generate microstructures of heterogeneous energetic materials. Although their network can successfully parametrize the microstructure features by conditioning on a global morphology parameter, periodic boundaries are not introduced, which poses a critical limitation in the calculation of the effective properties of piezoceramics using the FFT-based method. In addition, it is necessary and time-consuming for the patch-based GAN to find the right patch size (the receptive field size of a discriminator). Inappropriate choice of the patch size can result in an unstable optimization or a lower quality of images.[44] Andrea et al.[43] proposed to use GAN to generate multiphase electrode microstructures. Although they successfully generated microstructures with periodic boundaries by applying circular spatial padding to an input parameter, their model is not able to control the microstructure features. In addition, neither of them can achieve high-resolution microstructures with more details of the microstructure features because they obtain the microstructures of larger size by simply enlarging the input size. On the other hand, the StackGAN encourages drawing more details in higher-resolution images by capturing more information from conditional variables,[45] which is omitted in the stage of generating low-resolution images.

In this paper, a DL approach, multistage stacked generative adversarial network (Stack-GAN-v2),[40] is applied for the first time to generate high-fidelity microstructure models for BTO piezoceramics fabricated by an AM process. The presented modeling approach can reconstruct high-resolution microstructures for the piezoceramics through a hierarchical stack of conditional GAN models. More details such as the morphology of micropores and grain boundaries can be clearly identified. Highly variable yet statistical equivalence with experimentally observed AM-ed microstructures can be synthesized through a novel conditioning augmentation (CA) technique that presents the smoothness in the latent conditioning manifold.[40] Advantages of the proposed modeling approach are also illustrated from its capability in controlling the grain size and orientation, as well as the volume fraction (VF) and distribution of the micropores in a large space by manipulating intrinsic parameters of StackGAN-v2. This would have significant benefits in exploring these microstructure effects on the piezoelectricity of piezoceramics from the material-by-design aspect. In addition, in the developed microstructure models, periodicity of the microstructures has been successfully introduced, which would facilitate the using of FFT-based methods to efficiently predict the performance of the piezoceramics. In another word, the proposed DL modeling approach can interface with other computational methods in optimizing microstructures for the piezoceramics as well as other piezoelectric materials to achieve the desired piezoelectric and electromechanical properties.

2. METHOD

2.1. Training Images from Phase Field Grain Growth Model. DL models require large quantities of training data. Unfortunately, it remains a daunting challenge to collect the large quantities of experimental data in the community. Moreover, the experimental images usually involve a bunch of information or features, but some of them are insignificant and/or noises in nature due to the limitations of characterization techniques. Appropriate image processing such as segmentation and adjustments of pixels should be adopted for the training. On the other hand, simulation data are straightforward to use without any preprocessing and can be flexibly generated to focus on the most important features, e.g., grain size, volume fraction of pores, and grain orientation for AM-ed piezoelectric microstructures. In fact, it is common to use simulation images as the training data of deep learning[35,41,46,47] in material science and engineering. For instance, Singh et al.[46] used Cahn−Hilliard equation to generate microstructures for training and testing. Li et al.[35] employed a Gaussian random field (GRF) to synthesize microstructure patterns for the training sets.

In the present study, the training images are provided by the images generated in a previous work[4] by PFM to demonstrate the multistage StackGAN-v2 in generating microstructure images with high resolution, sufficient variability, high controllability, and guaranteed periodicity. These images were statistically reconstructed through the comparison between the PDFs of key features (e.g., grain size and number of neighboring grains) of the microstructures generated by PFM and those of scanning electron microscope (SEM)

https://doi.org/10.1021/acsami.1c12945
ACS Appl. Mater. Interfaces 2021, 13, 53439−53453

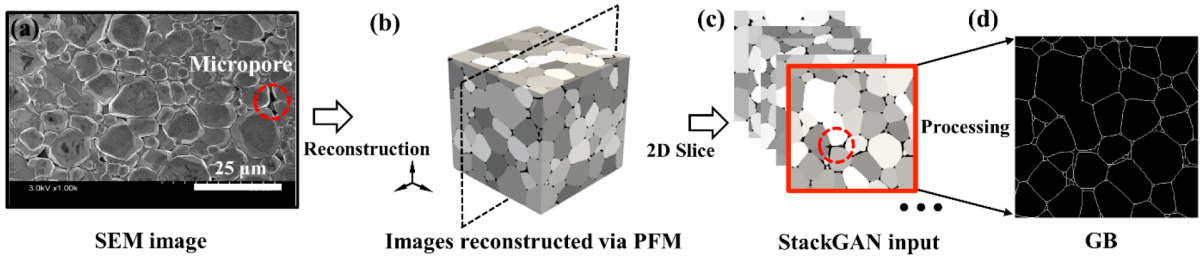

Figure 2. Images of the microstructure of piezoceramics: (a) an experimental image of AM BTO obtained by SEM, (b) a 3D microstructure statistically reconstructed by PFM in a previous work, (c) 2D images obtained by slicing from b, and (d) a GB obtained by image processing of the top image in c via *ImageJ*. Notice that a representative micropore along GB is marked by a red dashed circle in a and c.

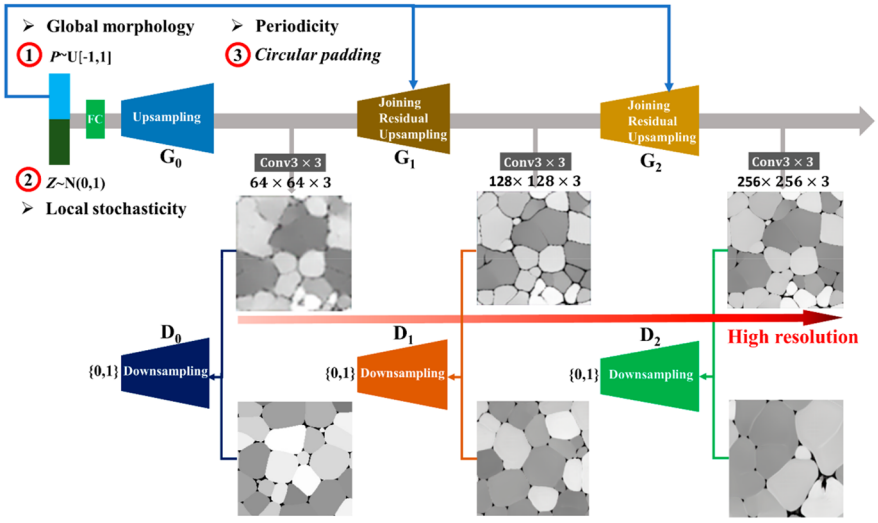

Figure 3. Architecture of StackGAN-v2 used in this work, where **P** is a constant vector and **Z** a noise vector. **P** is randomly drawn from a uniform distribution on the interval [−1,1], whereas **Z** is chosen from a normal distribution (0,1), where 0 and 1 are the mean and standard deviation of the distribution, respectively. G and D indicate the generator and discriminator at different stages, respectively.

images from the AM-produced BTO piezoceramics. Specifically, a total of 4848 2D images (Figure 2c) were acquired by slicing simulated 3D images (Figure 2b) along the *x*, *y*, and *z* directions, separately. Of these, 3848 images are used for training data sets, whereas the rest are for testing. These images were obtained by linearly mapping the Euler angles of grains to the color space. For instance, black corresponds to 0° and white to 360° of the Euler angle. Therefore, the orientations of grain could be distinguished by their discrepancy in colors. Images as presented in Figure 2c together with conditioning information on parameters **P** and **Z** will be used as the inputs for the training of StackGAN-v2. To verify that the microstructures generated by StackGan-v2 possess high stochasticity, we trained pix2pix for comparisons. pix2pix was developed based on the conditional GAN (CGAN)[38] as an approach to image-to-image transfer. The special design of its architecture intrinsically requires another image such as the GBs in this study as the condition information as well. The GBs (Figure 2d) were obtained by processing the 2D images (Figure 2c) using the widely adopted software *ImageJ*.[48−50] Specifically, the images obtained from the PF simulations were first transformed to 8-bit images of gray scale. Some GBs were first detected on the transformed gray scale images by finding the edges of grains, followed by thresholding to obtain all the GBs. The thresholded images were binarized with black and white color only, which were then skeletonized to obtain images with only GBs.

2.2. Microstructure Reconstruction via StackGAN-v2.

StackGAN-v2 developed by Zhang et al.[40] was modified for reconstructing the microstructures of piezoceramics. This DL-based method was upgraded based on a two-stage GAN (StackGAN) architecture developed by Zhang et al.[45] Unlike vanilla GAN,[37] the StackGAN has two stages, and each stage contains one generator (G0 or G1) and one discriminator (D0 or D1) as indicated in Figure 3. The generators at each stage are used to generate synthetic images of different resolutions, while the discriminators of their corresponding stage try to detect the synthetic images from the real ones of the same resolution. Specifically, at the first stage, the generator generates a preliminary sketch of a scene by entering a noise vector conditioned on a text describing the scene. At the second-stage GAN, the results obtained from the first stage and the same text as that used for the first stage are entered as inputs to produce higher-resolution images with much more detail. The StackGAN-v2 used in this study contains more stages and can thus generate higher-resolution images as compared with StackGAN. Moreover, StackGAN-v2 can be employed for both conditional and unconditional generative tasks and displays a more stable training behavior than the two-stage StackGAN does.

In this work, three stages or branches will be followed to generate high-resolution (256 × 256) images as illustrated in Figure 3. Specifically, the noise vector **Z** of size *m* will be conditioned on a constant vector **P** of size *n* in replacement of

https://doi.org/10.1021/acsami.1c12945
ACS Appl. Mater. Interfaces 2021, 13, 53439−53453

a vector of embedded text. The vector **Z** will then concatenate with **P** to form an input tensor of size $b + m + n$, in which b is the batch size. In particular, the noise vector **Z** is used to control the local stochasticity of the generated microstructures, whereas the vector **P** is employed to control the global morphology of the microstructures such as grain size and texture.[42]

- An input tensor will be linearly transformed at first by a fully connected (FC) layer and batch-normalized before entering the first stage, which consists of four upsampling layers of factor two through an interpolation layer. The channel of the resulting tensor will then be reduced to 3 by a convolution layer of 3 × 3 to construct 3 × 64 × 64 low-resolution images as illustrated in Figure 3.
- Next, the obtained images and the **P** vector will be convolved together before entering the second stage that contains two residual block layers and one upsampling layer of factor 2. Like the generator at the first stage, the channel of the output tensor will be compressed to 3 to generate 3 × 128 × 128 medium-resolution images (see Figure 3). In particular, the residual block layers are used as an encoder decoder network to correct incoherent artifacts or defects yielded in the low-resolution images.[40] Moreover, the noise vector **Z** will not be added at this stage because the stochastic nature has already been induced by this vector in the image generation at the first stage.
- The third stage has an identical setting as the second stage and can generate 3 × 256 × 256 high-resolution images as depicted in Figure 3.

It should be noted that circular padding is applied to the data in all convolution layers of the generators except for the first upsampling layer of the first stage. This circular padding will enforce periodic microstructures when calculating the convolution, which is essentially required for the FFT-based method to determine the piezoelectric performance of piezoceramics. This is because the FFT-based method requests a periodic boundary condition, which can be readily defined in periodic microstructures. The architecture of the discriminator is the same as that of the original conditional StackGAN-v2;[40] however, the **P** vector will not be convolved with images to calculate a conditional loss as the conditional StackGAN does. Specifically, for the discriminator at the first stage, the images are encoded 16 times through a series of convolutional layers followed by one 1 × 1 convolutional layer to jointly learn features across the image. Finally, a FC layer with the Sigmoid function as its activation function is used to make a decision-score with 0 as a fake and 1 as a real microstructure, as depicted in Figure 3. The architectures of the discriminators at the second and third stage are basically the same as that of the discriminator at the first stage with the exception that more down-sampling blocks are required on the stage 2 and 3 due to larger sizes of the images processed at those stages. Circular padding will not be applied to any layers of the discriminators throughout all the stages with an assumption that the generators with cycle padding can ensure the periodicity of microstructures.

2.3. Microstructure Characterization Metrics. The computationally generated synthetic microstructures must faithfully reflect the real microstructures to promote the application of computational methods in revealing the microstructure−property relationship of piezoceramics. Thus, qualitative and quantitative comparisons between the real and synthetic microstructures are necessary for validating the computational microstructure models. The qualitative comparison is more straightforward and can be implemented through visually inspecting the characteristics of key microstructure features (location and shape of micropores, the size and shape of grains, etc.). Although a quantitative study has to be conducted to compare the key features in the real and synthetic microstructures by employing both physical descriptors and statistical functions as microstructure characterization metrics.

2.3.1. Physical Descriptors. Physical descriptors such as the VF of micropores are easy to implement and can be directly applied for the mining process, the structure, and the property relation. For instance, using the VF of micropores in the AM BTO,[51] the relations behind the weight ratio between ceramic particles and polymer binders, microstructures with distinct VF of micropores due to different weight ratios, and various piezoelectric charging coefficients d_{33} corresponding to different microstructures can be developed. However, the physical descriptor method usually ignores important morphology and spatial correlation information such as the spatial distribution of micropores in the piezoceramics. In the present study, physical descriptors of the microstructure features which have significant effects on piezoelectric responses as indicated in the introduction will be adopted. Specifically, the VF of residual micropores, the PDF of grain sizes, the number of neighboring grains and grain orientations will be used as physical descriptors to quantify porous polygranular structures of AM piezoelectric materials.

The VF of micropores of each microstructure can be obtained by setting a threshold of a certain pixel value (e.g., 0.3), which can convert the microstructures to binary images with 0 and 1 representing micropore and grain phase, respectively. The ratio of the number of pixels with 0 value to total pixels in a microstructure would be the VF of micropores. The area of a grain in the microstructures were determined by counting the number of pixels located within the boundaries of that grain, and then an equivalent grain radius was defined to be the radius of a circle with the same area of that grain. The number of neighboring grains were obtained by analyzing each of the samples by Voronoi method. Specifically, all the physical descriptor analysis from microstructures can be done by *ImageJ*.[48−50]

2.3.2. Statistical Functions. Statistical functions such as correlation and lineal-path functions are compliant to the stochastic nature of the microstructures[12,52] and can be used to obtain systematic and rigorous descriptions of hierarchically internal microstructures. Therefore, the statistical functions are remarkably useful in microstructure characterization and verification of the reconstructed microstructures. In the present study, a two-point correlation function $S_2(r)$ and a lineal-path function $L_2(r)$ are used to characterize the morphology of heterogeneous media featured in the microstructures of piezoceramics. $S_2(r)$ aims at finding the probability V that the end points belong to the same phase q_i of interest (e.g., the micropore phase) when randomly tossing a line of distance r on the microstructures;[16,43] it is thus defined as

$$S_2(r) = V(x \in q_i,\ x + r \in q_i) \text{ for } x,\ r \in \mathcal{R} \tag{1}$$

$L_2(r)$ is similar to $S_2(r)$ except that its goal is to find the probability that all the points on the line are from the same

https://doi.org/10.1021/acsami.1c12945
ACS Appl. Mater. Interfaces 2021, 13, 53439−53453

phase q_i when throwing a line of distance r. Jointly, these two functions can capture spatial correlation and connectivity characteristics of the microstructure features so as to facilitate the understanding of their influence on the performance of piezoelectric materials.

2.4. FFT-Based Physical Simulation. Finally, the effective piezoelectric responses and their spatial distributions (e.g., piezoelectric charging constants d_{33}) would be compared between synthetic and real microstructures as a final assessment of the computational methods and models applied in this research. In particular, a Fourier spectral iterative perturbation method (FSIPM) based on FFT was adopted to solve the equilibrium equations in a periodic system because this method is an efficient and direct numerical algorithm.[53,54] An external electric field $E^{ext} = 2 \times 10^7$ (V/m) was applied in the poling direction with a stress-free mechanical boundary condition assigned. Poled BTO[11] was selected as the ceramic phase in this work because of its popularity as a lead-free piezoelectric material.

3. RESULTS AND DISCUSSION

The StackGAN-v2 was trained for 200 epochs with batch size of 12. Adam[55] solver with momentum term beta1 = 0.5 and a learning rate of 0.0002 for all models was adopted to optimize the hyper-parameters in the neural network model. Models saved at epoch 85 are used in the remaining parts because ithey outperform the models saved at the other epochs; see learning curves and microstructures generated periodically in Figures S4 and S5 in section C of the Supporting Information.

3.1. High-Resolution Microstructures with More Details. Figure 4 depicts synthetic microstructures of different resolutions generated by the generators of first stage, second stage, and third stage of StackGAN respectively (see Figure 4a–c). The real microstructure is also provided for the purpose of qualitative comparison. From that figure, it can be seen that the size, shape, and location of the grains in the polycrystals generated via the improved StackGAN, especially those observed in the high-resolution image generated by the third stage generator, closely resemble the real ones. In addition, the location and shape of micropores are successfully emulated, which mostly appear at the GBs with irregular shapes. Moreover, comparing the reconstructed microstructures with different resolutions, it can be found that a higher-resolution image is sharper and can provide more details on the GBs and the morphologies of micropores as depicted in the synthetic microstructure displayed in Figure 4c. This could be attributed to the encoding and decoding nature of the generators, and more information is learned from conditioning variables in the stages of higher resolution.[40] The capability to generate different resolutions of microstructures has advantages compared with the StyleGAN-based architectures,[56] which can only output microstructures fixed at the size of the training images. The ability to add more details of microstructure features demonstrates its superiority to those single-stage GANs[42,43] that can generate only images with various sizes but cannot add any details of microstructure features in the images of larger size; see Figure S1 in section A of the Supporting Information for more details. This superiority is enabled because of the hierarchical architectures of StackGAN-v2 through a sketch-refinement process[45] that rectifies defects and adds compelling details in the results of previous stages. The grain microstructures of piezoceramics containing more details of microstructure features can have many benefits. For instance, it can enhance the simulation accuracy when predicting the effects of these microstructure features on the effective piezoelectric properties.

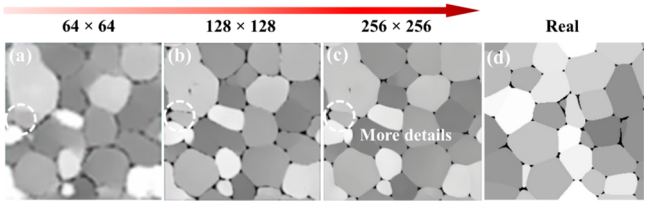

Figure 4. Comparison between (a–c) synthetic microstructures with resolutions of 64 × 64, 128 × 128, and 256 × 256, respectively, and (d) the real microstructure. Notice that more details such as the morphologies of micropores are reflected in the higher-resolution images as marked by a white dashed circle.

3.2. Microstructures with Periodicity. Polycrystals with periodicity in four directions, i.e., four edges of the image are successfully generated as presented in first two columns of Figure 5. A real microstructure (last two columns of Figure 5) without periodicity is also presented for comparison. As mentioned above, the periodicity of the reconstructed microstructures is induced by adding the circular padding in the generators except for the first upsampling layer. During the calculation of the material properties, e.g., piezoelectric properties of piezoceramics using FSIPM in the present study, RVEs of the microstructures together with periodic boundary conditions are often used to save computing time and efforts.[4,18,57,58] It is noted that a microstructure without periodic boundaries cannot be used as an RVE. This is because the grains at left/right or top/bottom edges of the microstructure cannot be combined into the same grains, when the grain structure is joined as a periodic unit cell, as marked by red dashed circles in the last two columns of Figure 5. On the other hand, the grains at the four edges of synthetic structures can form into the same grains, respectively, because they are complementary with other in terms of grain shape, and have the same color (i.e., pixel value) as indicated in the red circles in the first two columns of Figure 5. The microstructures with

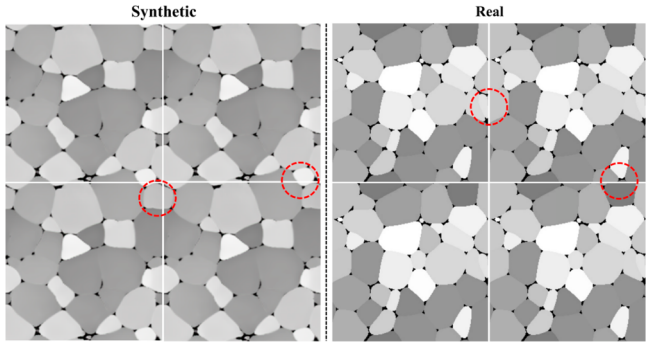

Figure 5. Illustration of periodicity in a synthetic microstructure (the first two columns) along four directions. A real microstructure generated by PFM with no periodicity is shown in the last two columns for comparison. Notice that the 2 × 2 array of the images consists of images for the same real or synthetic microstructure. The red circles indicate the grains at the top and bottom or left and right edges of the microstructure that can (for synthetic) or cannot (for real) form into a grain, respectively.

https://doi.org/10.1021/acsami.1c12945
ACS Appl. Mater. Interfaces 2021, 13, 53439–53453

periodic boundaries can significantly reduce the simulated volume size of the microstructures considered to be the RVE of an original microstructure. Therefore, the periodic microstructures can make these simulations more efficient, which enable them as ideal candidates for materials design and optimization.[43]

3.3. Microstructures with High Variability Yet of Statistical Equivalency. The images generated by the multistage StackGAN are not simply copies of the training images but through learning a representation of the high-dimensional probability distribution underlying the images space from the training data sets. This section will demonstrate that the microstructures generated by StackGAN-v2 shows high variabilities and are statistically equivalent to the real microstructures from testing data sets in terms of key physical descriptors and statistical functions. On the contrary, the images generated by the pix2pix look like copies of the training images, i.e., almost no stochasticity in terms of grain size and grain orientation can be observed in the output from pix2pix (see Figure 6). This phenomenon could be attributed to that

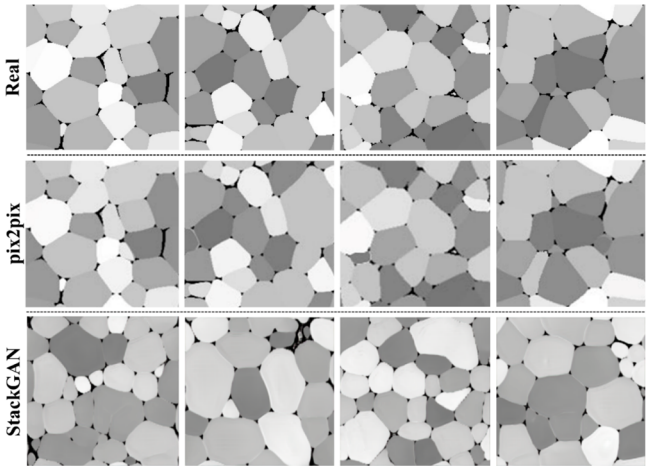

Figure 6. Comparison between real microstructures (top row) and synthetic structures generated by the pix2pix (mid row) and StackGAN-v2 (bottom row). Notice only minor stochasticity can be observed in the synthetic microstructures generated by pix2pix.

the generator learned to ignore the noise vector **Z** due to the conditional data (e.g., GB in the present study) is complicated enough to provide sufficient information to the generator.[39] Thus, the noise vector **Z** is not able to provide stochasticity in the synthetic microstructures, resulting in merely deterministic outputs. On the other hand, the multistage StackGAN-v2 enables the variability of synthesized images that are statistically equivalent with experimentally observed AM-ed piezoelectric microstructures, through a novel conditioning augmentation (CA) technique that presents the smoothness in the latent conditioning manifold;[40] see Figure S2 in section A of Supporting Information for more details. Since exploring the space of material morphologies is critical to the investigation of the microstructural effects on the piezoelectric properties, only the results generated by the multistage StackGAN-v2 will be discussed in later sections.

3.3.1. In Terms of Physical Descriptors. The statistical equivalence between the real and synthetic microstructures can be compared in terms of some key physical descriptors such as the VF of micropores and PDFs of normalized grain areas and radius, and PDFs of a number of neighboring grains and crystal orientations, as presented in Figure 7a. The curves and columns in that figure were plotted based on average values of the corresponding physical descriptors of 100 samples of real and synthetic microstructures; see Figure S6 in section D of Supporting Information for comparison results using 500 samples. Those samples were randomly chosen from the testing data sets of real and synthetic microstructures to allow for a statistically meaningful comparison. The average VF of pores is 5.89% with a standard deviation of 0.016 for the real microstructures and 5.52% with the standard deviation of 0.013 for the synthetic microstructures. As can be seen from the Figure 7a, the PDFs of the normalized grain area and radius, and the number of neighboring grains obtained from the real and the synthetic microstructure closely agree well with each other. Those values are well fitted by log-normal distribution functions (Figure 7(a)), which match agreeably with the curves obtained from experiments.[57] Crystal orientations of each microstructure were obtained using the method described in subsection 3.3.3. As presented in Figure 7a, the PDFs of crystal orientations have a close match with each other. In particular, those values are well fitted by normal distribution functions, which indicates both the real and synthetic microstructures exhibit a low texture with almost random distribution of crystal orientation. But as will be demonstrated in subsection 3.4, the crystal orientation can be easily controlled to achieve grain microstructures of different textures.

3.3.2. In Terms of Statistical Functions. $S_2(r)$ and $L_2(r)$ of the micropore phase between the real and synthetic microstructures were compared using the same samples as those used in comparing physical descriptors (Figure 7b). The graphs were plotted using the mean values of the $S_2(r)$ and $L_2(r)$ of the real and synthetic microstructures, separately. As can be seen from Figure 7b, statistical functions obtained from the synthetic microstructures match with those of the real ones very well. Although there are some deviations from the statistical functions of the real microstructures, those deviations are still within the ranges of standard deviations of the statistical functions of the real microstructures. In particular, the range of the standard deviation of the statistical function of the synthetic microstructures is wider than that of the real microstructures. This indicates that the multistage StackGAN has successfully learned a representation of a high-dimensional probability distribution from the training images that are a representative sample of the probability distribution underlying the image space.[37] This would be extremely valuable for studying the microstructure effects on the piezoelectric properties as will be demonstrated in section 3.4. In addition, since the microporosity VFs in both the real and synthetic microstructures are low, as the pixel distance r increases, the probability of finding that the two end points of a line with a distance r belong to the micropore phase becomes more difficult. When the distance reaches 30 pixels, it becomes almost impossible to find these two end points on a line belongs to the micropore phase. This phenomenon becomes more obvious for the lineal-path function because the lineal-path function requires all points within the line belong to the micropore phase. As shown in the right graph of Figure 7b, the probability of finding all the points in that line is almost zero when the distance exceeds 20 pixels.

Therefore, through both the qualitative and quantitative comparison between the real and synthetic microstructures, it

https://doi.org/10.1021/acsami.1c12945
ACS Appl. Mater. Interfaces 2021, 13, 53439−53453

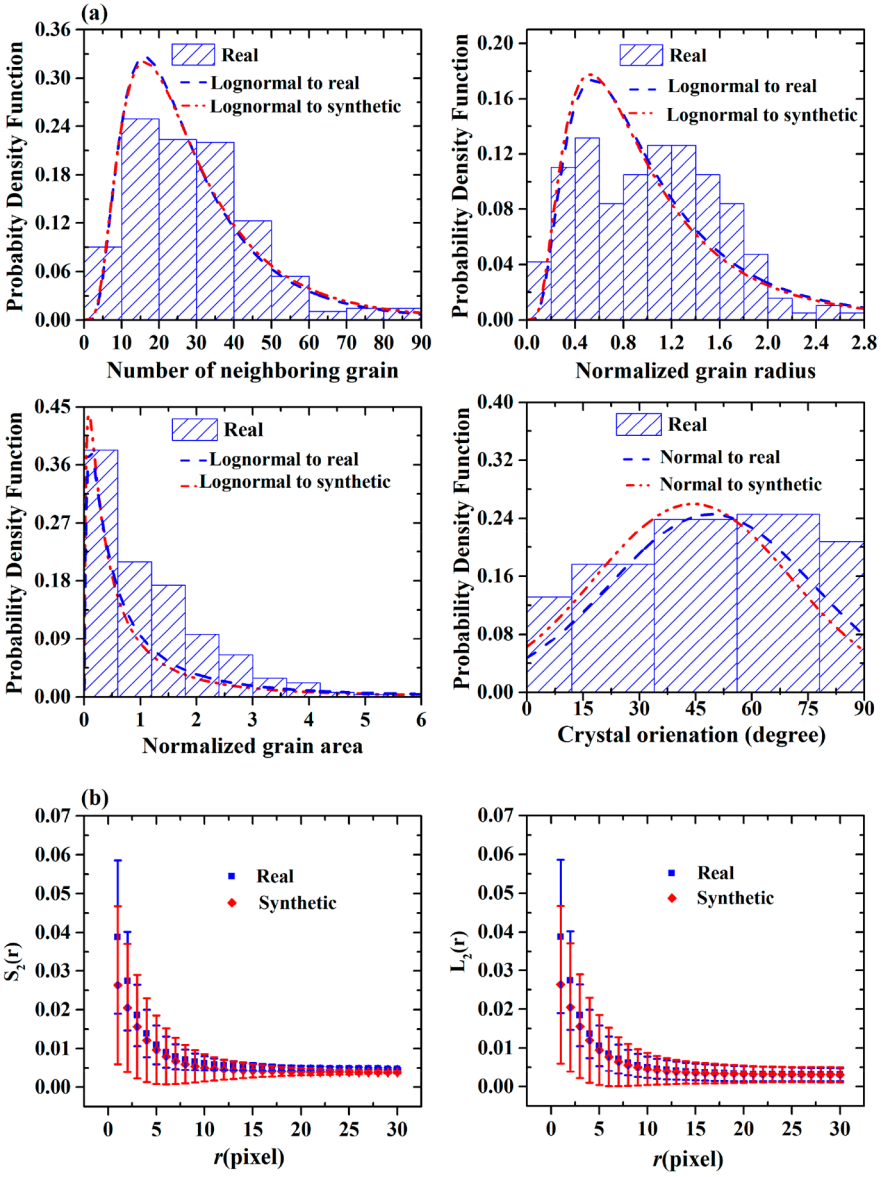

Figure 7. Comparison between real and synthetic microstructures in terms of (a) physical descriptors and (b) statistical functions.

has been proved that the improved StackGAN successfully learned the statistics of microstructure features in the real microstructures. In particular, the synthetic microstructures exhibit a higher variance in all the comparison metrics compared with those of real ones.

3.3.3. In Terms of Piezoelectric Response. This section focuses on the effects of the microstructure features that exist in the piezoceramics fabricated using both the traditional[59,60] and AM process[4] on their piezoelectric responses. In this study, the piezoelectric responses are indicated by the piezoelectric charging constant d_{33} and relative permittivity κ_{33}. Figure 8 compares d_{33} calculated based on the real microstructure and a high-fidelity one generated using the multistage StackGAN. Their PDFs of key physical descriptors (e.g., grain orientation), statistical functions, and VFs of micropores are close to each other. In particular, the grain orientations in piezoceramics are described by three independent Euler angles (θ, ψ, ξ),[7,13,14] which correspond to three consecutive counterclockwise rotations with respect to the global coordinate (x_1, x_2, x_3), as θ about the x_3-axis, ψ about the rotated x_1'-axis, and ξ about the newest x_3'-axis. The pixel value of each grid point in a grayscale image in PNG format (first column of Figure 8) ranges from 0 (black) to 1 (white), whereas the ψ value of each grid point ranges from 0 to 360°. Therefore, ψ of each grid point can be obtained by multiplying the pixel value of that grid point with 360°. The angle ξ can be obtained by solving the following equation.

$$F(\xi) = 0.5 \cdot [1 - \cos(\xi)] \tag{2}$$

Where F has a uniform distribution ranging from 0 to 1, ξ is no greater than 180°, and θ equals to a value randomly chosen from the interval [0,1] multiplied by 360°. In addition, both ξ and θ are uniform for a same grain. Through mapping the pixel values of all the grid points to the corresponding Euler angles ψ, a distribution of pixel values could be transformed to an appropriate distribution of grain orientations. Notice that the Euler angles can be transformed to acute angles according to the equation as below when considering the poling process; see

https://doi.org/10.1021/acsami.1c12945
ACS Appl. Mater. Interfaces 2021, 13, 53439−53453

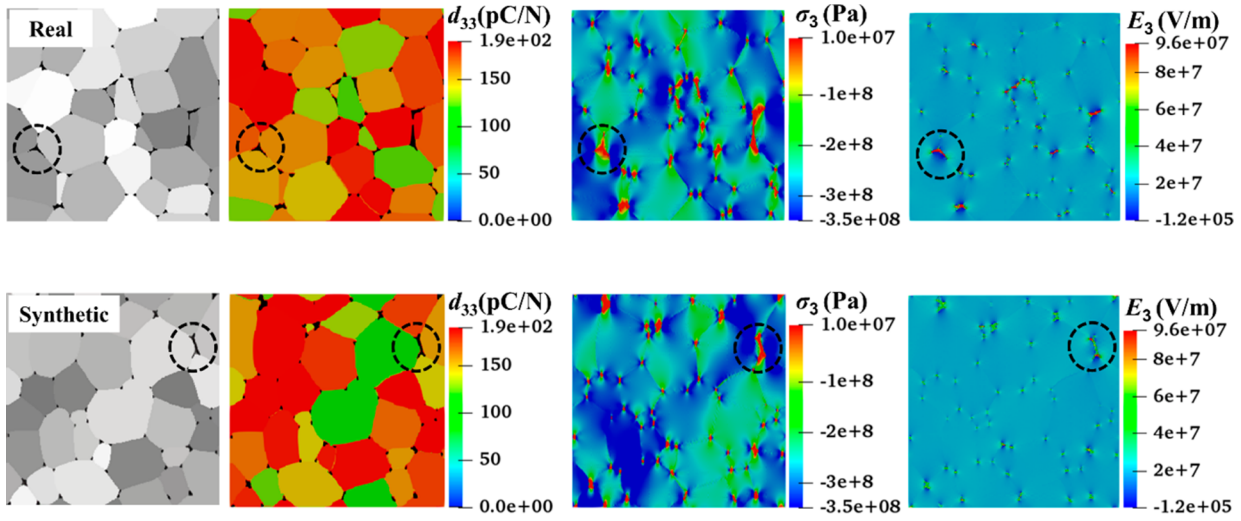

Figure 8. Calculated spatial fields of d_{33} for real (top) and synthetic (bottom) grain structures. Longitudinal stress σ_3 and internal longitudinal electric field E_3 are induced nearby micropore areas, such as the ones marked with black dashed circles.

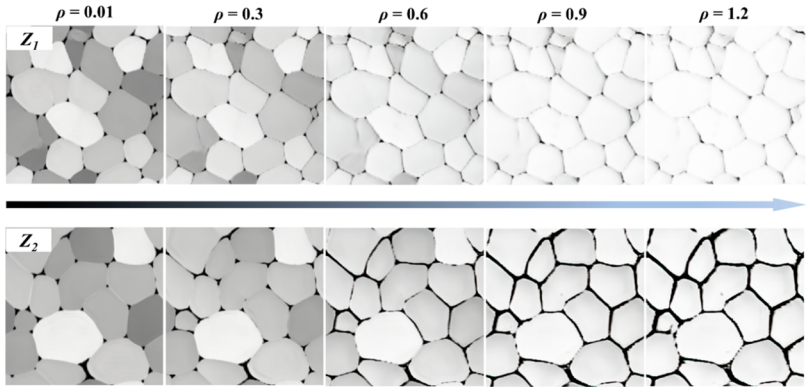

Figure 9. Fine tuning the characteristics of microstructure features (crystal orientation and VF of porosity) by manipulating the standard deviation ρ of **P** parameters.

section B of the Supporting Information for the details of poling process.

$$\cos(x) = |\cos(x)| \tag{3}$$

Thus, the three Euler angles can be assigned to each grid point in the real and synthetic microstructures using the method described above. By employing the FSIPM method as described in subsection 2.4, the effective d_{33} and κ_{33} of the real and synthetic microstructures can be calculated. Specifically, the effective d_{33} is found to be 152.3 and 152.1 pC/N, whereas the effective κ_{33} is 1529 and 1556 for the real and synthetic microstructure, respectively. As seen in the third and fourth column of Figure 8, the calculated spatial distributions of the longitudinal stress σ_3 and the internal longitudinal electric field E_3 of the real and synthetic grain structures are identical. In particular, the concentration of these two fields can be observed near the interface between the micropores and grains, which are positive in micropores and negative in their neighboring grains as marked by a black dashed circle. This phenomenon contributes negatively to effective d_{33} and may be attributed to the large mismatch of the κ_{33} and d_{33} between micropores and neighboring grains.[7,14]

The identical results obtained from the real and synthetic grain microstructures confirm that the multistage StackGAN is capable of effectively learning the data distribution of microstructure features and precisely capturing their details. Therefore, the microstructures reconstructed using the multistage Stack-GAN can replace the real microstructures for studying the microstructure−property−performance relationship of piezoceramics and their composites.

3.4. High Controllability of Microstructures: An Ingredient toward Materials-by-Design. The capability to control micromorphology in the large underlying space by StackGAN-v2 can greatly help the optimal design of piezoceramic materials, which is enabled by taking advantage of the achieved high variability in microstructures. Specifically, the PDFs of microstructure features can be tuned conveniently by manipulating the parameter **P** and/or **Z**. While ***P*** can be used to control the global micromorphology and ***Z*** to control stochastic variations in the microstructure.[42]

*3.4.1. Microstructure Control via Parameter **P**.* During training, the numerical value of each element in **P** is set as the same constant drawn from a uniform distribution on the interval $[-1,1]$. However, at inference time, microstructures with distinct PDFs of the microstructure features can be obtained by assigning each element in **P** with a different value. This can be easily done by drawing the values from a normal distribution (μ, ρ), where μ and ρ represent mean and standard deviation of the distribution, respectively. Some representative microstructures that generated by setting μ and

https://doi.org/10.1021/acsami.1c12945
ACS Appl. Mater. Interfaces 2021, 13, 53439−53453

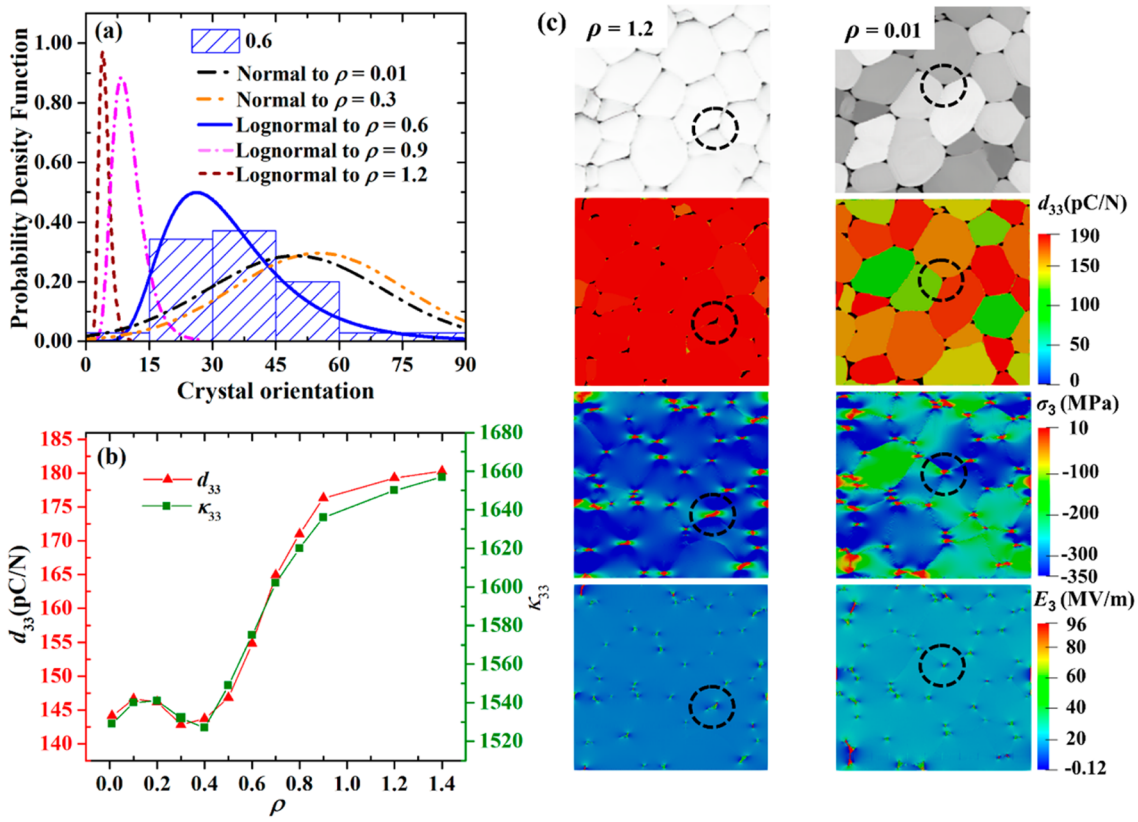

Figure 10. (a) High controllability of the PDFs of crystal orientation of grain microstructures by manipulating the standard deviation ρ of parameter **P**. (b) Distinct PDFs of crystal orientations induce dramatic change in piezoelectric properties. (c) Illustrates the spatial field distributions of longitudinal σ_3 and E_3 of the two grain microstructures that have different PDFs of crystal orientation and were obtained by assigning a different value (ρ = 1.2 or 0.01) to the standard deviation ρ of **P** parameters.

ρ as 0.1 and 0.3, respectively, are presented in the Figure S7 of section E of Supporting Information. Herein, we demonstrate the high controllability of the PDFs of two important microstructure features by varying the value of ρ after selected two appropriate vectors $\mathbf{Z}_1$ and $\mathbf{Z}_2$. Moreover, the significant effects of these two features on piezoelectric properties and their underlining mechanisms will be discussed. Through this, the full potential of proposed approach for optimal microstructure design of piezoceramics can be sufficiently demonstrated.

Specifically, two groups of grain microstructures with wide range of PDFs of crystal orientation or VF of micropores were synthesized. Several of these two series of microstructures are illustrated in Figure 9, which display the gradual change of the crystal orientation (first row) and VF of micropores (second row), respectively. As seen, the crystal orientations of the grain microstructures of the first row of Figure 9 become increasingly uniform due to the color of the images smoothly turn to white. The change of color (pixel value) arouses a corresponding variation of Euler angles based on the mapping relation as discussed in section 3.3.3. This would subsequently alter the PDFs of crystal orientation and thus the corresponding piezoelectric properties. Similarly, the VF of micropores of the second row become larger with the increase of the value of ρ. Moreover, the increment of micropores mainly occurs at the GB, which is the main characteristic of micropore distribution of the real microstructures. Notice that the grain sizes of these two series of grain microstructures remain almost unchanged. This allows for the high controllability of the characteristics of specific microstructure feature, thus pave the way toward materials-by-design.

Although the qualitative relation between the distribution of crystal orientation and ρ were discussed in last paragraph, the quantitative relationships between ρ and the crystal orientations of the microstructure features (see first row of Figure 9) are depicted in the Figure 10a. Of particular note is that the crystal orientations are represented by the Euler angles ψ, which are obtained by multiplying the pixel value of the images as discussed in section 3.3.3. Moreover, considering the poling effect, the Euler angles ψ have been converted to acute angles using eq 3. As seen in Figure 10a, significantly different crystal orientations can be achieved by controlling the value of ρ. Specifically, with the increasing of the value of ρ, the PDFs of crystal orientation change from normal distribution to log-normal distribution. The normal distribution indicates the randomness of the crystal orientations, whereas the log-normal distributions imply that finding the Euler angle ψ that are less than 45° has much higher chance. The immense difference in the PDFs of crystal orientation may induce significant piezoelectric properties of piezoceramics. The piezoelectric responses of the grain microstructures including those in the first row of Figure 9 were calculated using FSIPM method and the results are presented in Figure 10b. As can be observed, starting from ρ = 0.4, with the increasing of the value of ρ, the effective piezoelectric charging constant d_{33} and relative permittivity ε_{33} increase dramatically. This is because of the PDFs of crystal orientation lean toward left side gradually with the increasing of the value of ρ. The extent of differences in

https://doi.org/10.1021/acsami.1c12945
ACS Appl. Mater. Interfaces 2021, 13, 53439−53453

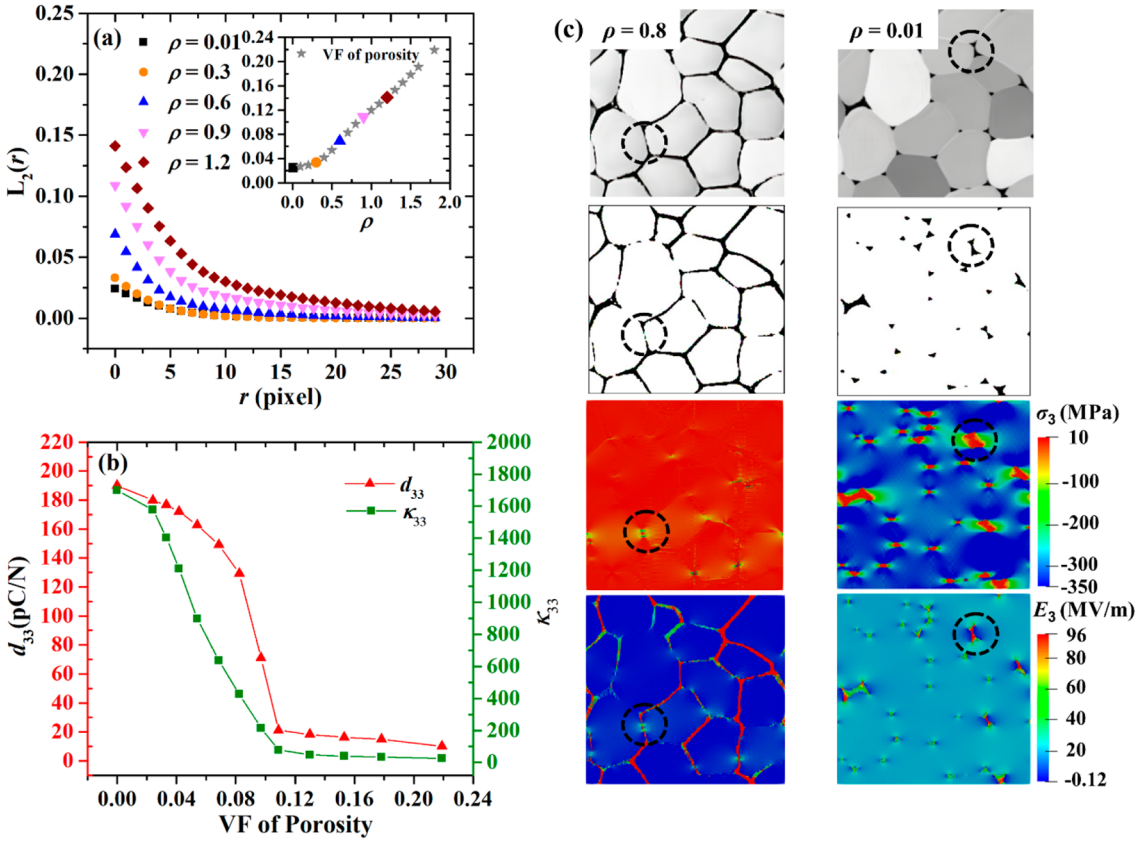

Figure 11. (a) High controllability of the lineal-path statistical functions of the grain microstructures by manipulating the standard deviation ρ of parameter **P**. This would control the VF of micropores simultaneously as shown in the inset graph. The great controllability of VF of micropores can provide convenient way to desired piezoelectric property as shown in b. (c) Illustration of the underlining mechanisms for the effect of micropores on piezoelectricity.

piezoelectric properties of grain microstructures are closely reflected the resemblance in their PDFs of crystal orientation. For instance, the PDFs of crystal orientation for ρ = 1.2 and ρ = 0.9 are close to each other, this results the similarity in their d_{33}. On the other hand, due to the larger difference in the PDFs of crystal orientation for ρ = 0.6 and ρ = 0.9, their discrepancy in d_{33} (154.8 and 176.3 pC/N) is relatively high. In addition, the d_{33} (142.8 pC/N) of the grain microstructure for ρ = 0.3 is slightly smaller than that (144.1 pC/N) for ρ = 0.01. This is attributed to the extent the PDF of crystal orientation for ρ = 0.3 leans toward left is mildly smaller as compared with that of ρ = 0.01.

To fully understand the mechanism through which the PDFs of crystal orientation affect the piezoelectric properties, the spatial distribution fields of two grain microstructure (ρ = 1.2 and ρ = 0.01) from the first row of Figure 9 were plotted and presented in Figure 10(c). By comparing their spatial fields of d_{33}, the field of the grain microstructure (ρ = 1.2) is significantly stronger and more uniform than that of the other grain microstructure. The less uniform field of d_{33} will induce a higher longitudinal stress σ_3 and a stronger internal longitudinal electric field E_3 as can be observed by comparison of these two spatial fields of them (see last two rows of Figure 10c), respectively. This is because of the strong mismatch of the d_{33} values between the neighboring grains. These two fields (σ_3 and E_3) will have detrimental effects on the materials' piezoelectric responses,[7] thus result in significantly distinct effective d_{33} values in the two grain structures.

The quantitative relation between the ρ and lineal-path statistical function $L_2(r)$ are established in Figure 11a based on the grain microstructures of the second row of Figure 9. Overall, the higher the value of ρ, the more probable to find the phase of micropores in the grain microstructures. With the increasing of the length of line segment (r value), the probabilities of finding all phases belong to micropores are decreasing. In addition, the statistical functions have similar shape due to the only difference in microstructure features between those grain microstructures are the VF of micropores, while the characteristics of the other microstructure features (e.g., grain size) are identical. The VF of micropores of those microstructures can be obtained from the value of statistical functions when the r equals to 0. The inset graph in Figure 11a depicts the relations between VF of micropores and the ρ, where some points that correspond to the symbols of statistical functions are marked by same color and shape. From the inset graph, the higher the value of ρ, the higher VF of porosity can be concluded. Starting from ρ = 0.4, they have almost linear relation with each other. Thus, the ρ of P can be used to conveniently to control the VF of micropores of grain microstructures, which takes only a millisecond using the trained generator of StackGAN-v2.

To unravel the relation between the piezoelectric response and VF of micropores, the piezoelectric response of the grain microstructures including those shown in the second row of Figure 9 were calculated using the FSIPM method and the results are presented in Figure 11b. Before the calculation, the

https://doi.org/10.1021/acsami.1c12945
ACS Appl. Mater. Interfaces 2021, 13, 53439−53453

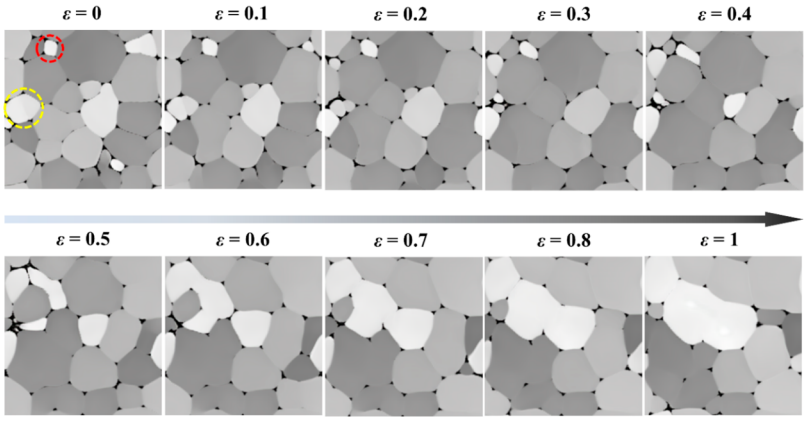

Figure 12. Linear interpolation between two noise vector $\mathbf{Z}_1$ and $\mathbf{Z}_2$. The smooth transition of the microstructure features indicates that the mode collapse does not exist.

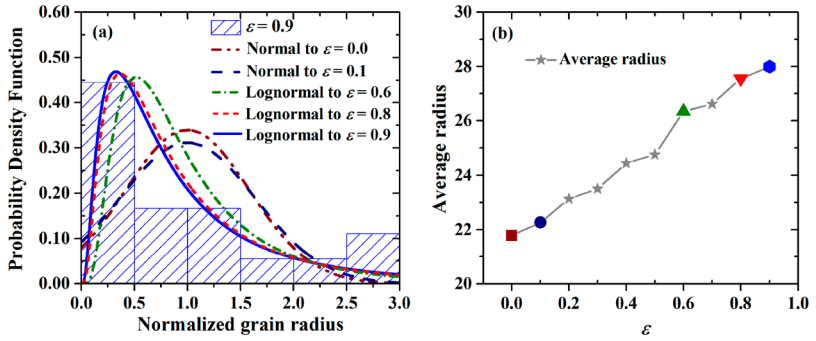

Figure 13. (a) High controllability of the PDF of normalized grain radius by varying the value of ε during the linear interpolation of two noise vectors. (b) Relations between the average of the grain radius and ε.

images were processed by thresholding to the ones with only black and white color that correspond to micropores and BTO piezoceramics, respectively. Through the thresholding, only the effects of micropores on piezoelectric properties will be evaluated. From the Figure 11b, the piezoelectric properties are severely deteriorated by micropores can be concluded. Overall, the porosity has stronger effect on ε_{33} as compared with that on d_{33}, although at 0.109 VF of micropores both reduced to only about 10% of those of the dense grain microstructures. Moreover, when the VF of porosity is greater than 0.083 (ρ = 0.7), d_{33} start to decrease rapidly. To understand this phenomenon, the spatial fields of the two grain microstructures (ρ = 0.8 and 0.01) were plotted and presented in Figure 11c. Concentration of longitudinal stress σ_3 and internal longitudinal electric field E_3 can be observed nearby the micropores. This may be attributed to the existence of micropores that lead to strong mismatch of local d_{33} between the pores and the neighboring grains. The mismatch will in turn induce the longitudinal stress σ_3 and internal longitudinal electric field E_3, which have negative effects on the piezoelectric responses as describe in previous paragraphs. The fields σ_3 and E_3 of the grain structure with a higher porosity level are much stronger than those of the grain structure with a lower porosity level as reflected in the last two rows of Figure 11c, which results in significant declines in piezoelectric properties. In addition, from the perspective of the connectivity of piezoactive phase, some grains start to become isolated from other grains when certain VF of micropores reached, as can be observed in the grain microstructure from the first two images of first column of Figure 11c. The connectivity of piezoactive phase (BTO) is thus significantly weakened, resulting in a severely decreased effective d_{33}.

3.4.2. Microstructure Control via Parameter Z. Although the PDF of crystal orientation and VF of micropores can be conveniently and rapidly controlled by ρ, noise vector $\mathbf{Z}$ could be used to manipulate the PDFs of another important microstructure feature, i.e., grain size.[11,61] Specifically, the microstructure features can be fine-tuned by the linear interpolation of two noise vectors $\mathbf{Z}_1$ and $\mathbf{Z}_2$ through $y(\varepsilon) = \varepsilon\mathbf{Z}_2 + (1 - \varepsilon)\mathbf{Z}_1$ while fixing the vector $\mathbf{P}$. Through the interpolation, a smoothly varying range of microstructures can be generated as depicted in Figure 12. It should be noted that when ε = 0 or 1, the first and last microstructure in the figure can be obtained, respectively. The smooth transition of microstructure features is illustrated by the grain marked with a red dashed circle. As can be seen, the grain grows smoothly with the ε increasing from 0 to 1 until it combines with other grains to form a larger grain, although the grain marked with a yellow dashed circle shrinks continuously until its place is occupied by other grains. It is worth pointing out that the capability of generating a smooth variation in the microstructure suggests the inexistence of mode collapse in which low variability in the generated images can be observed when different inputs (e.g., noise vector $\mathbf{Z}$ in the present study) are inputted into the generators. In other words, the generator converges to a state that consistently generates identical synthetic microstructures; see Figure S2 of section A in the Supporting Information. This inexistence of mode collapse indicates that the generator of StackGAN-v2 does not memorize the training data, instead, it learns the underlying

https://doi.org/10.1021/acsami.1c12945
ACS Appl. Mater. Interfaces 2021, 13, 53439−53453

latent data distributions from high-dimensional data (e.g., images of grain microstructure in the present study).[43,62]

The capability to span the spaces of microstructure by the interpolation of noise vector can be fully utilized to control the physical descriptors such as the PDFs of normalized grain size and average grain radius as depicted in Figure 13. These statistics were obtained by analyzing the microstructures presented in Figure 12. Specifically, by analyzing Figure 13a, with the increasing of ε, PDFs will transfer from normal distribution to log-normal distribution. Simultaneously, the average grain radius become increasingly larger as seen in Figure 13b. Therefore, the characteristics of grain size can be easily controlled through the interpolation of two noise vectors. This high controllability would not be easy to achieve by using other types of machine-learning-based methods;[35,42] see Figure S3 of section A in Supporting Information. Many work has been devoted to find the dependence of piezoelectric properties on grain size, however, there are still large discrepancies in the literature.[61] With the sedulous research going on, the high controllability of the grain size of piezoceramics can greatly facilitate better understanding of the mechanisms of the grain size effect on piezoelectric properties.

4. CONCLUSION

In this study, a novel DL-based multistage StackGAN methodology is established for the reconstruction of synthetic microstructures of AM piezoceramics. Results from the qualitative and quantitative comparisons show that the reconstructed microstructures via this DL-based approach are statistically equivalent to the real ones. More details of the microstructure features such as micropore morphology can be added in higher-resolution images. Also, the images generated using StackGAN-v2 outperform the images generated using other state-of-the-art methods in precisely and completely capturing all features in the real microstructures. Another strength of the proposed DL-based microstructure reconstruction method is that such a method allows for the generation of microstructures with periodic boundary conditions. The FFT-based numerical methods such as FSIPM then can be readily applied on such microstructure models to determine material properties. Moreover, it has been verified that the proposed StackGAN-v2 method is capable of expanding the range of morphological variation. The variation ranges of the features in the generated microstructures (e.g., crystal texture, grain size, porosity VF) are much wider than those of the features in the real microstructures. In addition, the proposed method can precisely control the PDFs of microstructure features by manipulating **P** and/or **Z** vectors with the StackGAN-v2 method. All these traits make the presented StackGAN-v2 method an effective and powerful tool in investigating the structure−property−performance relationship of the piezoelectric materials (Figures 11 and 12).

Through the calculations of piezoelectric properties on a large ensemble of the morphology-controlled microstructures, the quantitative relations between the microstructure features and the piezoelectric properties and responses could be established by coupling with machine-learning models.[47,63] This would pave the way to quantify the effect of the microstructure stochasticity and/or uncertainty on the piezoelectric properties, i.e., structure−property relation, in a statistical fashion. The high controllability to generate the microstructure morphologies opens a new avenue to optimize piezoceramics and their composites to achieve desired piezoelectric and electromechanical properties by searching the microstructure morphologies in the large space. The results of this study will benefit industry because the piezoceramics and piezocomposites have been widely used in transducers,[2,64] biomedical applications,[65,66] and other wearable electronics for a wide range of applications including mechanical sensing[67,68] and energy harvesting.[1] On the basis of the outcomes of this study, a continued research of linking process, structure, property, and performance for AM piezoceramics and piezocomposites is underway, which will lead to guidelines of acquiring those piezoelectric materials with optimal properties by choosing appropriate AM processes and process parameters.

■ ASSOCIATED CONTENT

Supporting Information

The Supporting Information is available free of charge at https://pubs.acs.org/doi/10.1021/acsami.1c12945.

Comparison with c-DCGAN in terms of resolution, variability, and controllability; poling process; learning curves; evaluation of statistical equivalency with more samples using physical descriptors; miscellaneous microstructures generated by modified StackGAN-v2 (PDF)

■ AUTHOR INFORMATION

Corresponding Authors

Lei Chen − *Department of Mechanical Engineering, University of Michigan−Dearborn, Dearborn, Michigan 48128, United States; Michigan Institute for Data Science, University of Michigan, Ann Arbor, Michigan 48109, United States;* orcid.org/0000-0002-3053-7373; Email: leichn@umich.edu

Yucheng Liu − *Department of Mechanical Engineering, Mississippi State University, Mississippi State, Mississippi 39762, United States*; Email: yucheng.liu@sdstate.edu

Authors

Wenhua Yang − *Department of Mechanical Engineering, Mississippi State University, Mississippi State, Mississippi 39762, United States*

Zhuo Wang − *Department of Mechanical Engineering, University of Michigan−Dearborn, Dearborn, Michigan 48128, United States*

Tiannan Yang − *Department of Materials Science and Engineering, Pennsylvania State University, University Park, Pennsylvania 16802, United States;* orcid.org/0000-0002-2071-4778

Li He − *Department of Industrial and Systems Engineering, Iowa Technology Institute, University of Iowa, Iowa City, Iowa 52242, United States*

Xuan Song − *Department of Industrial and Systems Engineering, Iowa Technology Institute, University of Iowa, Iowa City, Iowa 52242, United States;* orcid.org/0000-0002-7353-4252

Complete contact information is available at: https://pubs.acs.org/10.1021/acsami.1c12945

Author Contributions

L.C. and Y.C.L. conceived the idea and designed the research. W.H.Y wrote the text of the paper. T.N.Y. helped the FFT-based method for piezoelectric property calculation. L.H. provided the experimental data. Z.W. helped revise the paper

and prepare the figures. W.Y.H implemented the deep learning modeling related work. All authors reviewed and approved the paper.

Notes

The authors declare no competing financial interest.

■ ACKNOWLEDGMENTS

The research is financially supported by Propelling Original Data Science (PODS) Grants from Michigan Institute of Data Science (MIDAS) and National Science Foundation (NSF) Grant CMMI-2020527 and startup funds from Department of Mechanical Engineering at University of Michigan-Dearborn. W.H.Y. and Y.C.L. acknowledge the support by NSF grant CMMI-1662854. The extensive simulations were supported through computational resources and services provided by the Center for Advanced Vehicular Systems (CAVS) at Mississippi State University. L.H. and X.S. acknowledge the support by NSF grant CMMI1825962.

■ REFERENCES

(1) Bowen, C. R.; Kim, H. A.; Weaver, P. M.; Dunn, S. Piezoelectric and Ferroelectric Materials and Structures for Energy Harvesting Applications. *Energy Environ. Sci.* **2014**, *7* (1), 25−44.

(2) Ramesh, R.; Kara, H.; Bowen, C. R. Finite Element Modelling of Dense and Porous Piezoceramic Disc Hydrophones. *Ultrasonics* **2005**, *43* (3), 173−81.

(3) Song, X.; He, L.; Yang, W.; Wang, Z.; Chen, L. Co-Continuous Piezocomposites with Triply Periodic Phase Interfaces for Enhanced Mechanical Flexibility and Piezoelectricity. In *International Manufacturing Science and Engineering Conference*; American Society of Mechanical Engineers: New York, 2018; Vol. *51357*, p V001T01A020.

(4) Song, X.; He, L.; Yang, W.; Wang, Z.; Chen, Z.; Guo, J.; Wang, H.; Chen, L. Additive Manufacturing of Bi-Continuous Piezocomposites with Triply Periodic Phase Interfaces for Combined Flexibility and Piezoelectricity. *Journal of Manufacturing Science and Engineering* **2019**, *141* (11), 111004.

(5) Shen, J.; Wu, R.; Shen, M.; Wei, Y.; Lei, L.; Chen, L.; Yang, X.; Jin, Z.; Xu, S.; Gou, Z. Effect of Foreign Ion Substitution and Micropore Tuning in Robocasting Single-Phase Bioceramic Scaffolds on the Physicochemical Property and Vascularization. *ACS Applied Bio Materials* **2020**, *3* (1), 292−301.

(6) Min, L.; Zhang, H.; Pan, H.; Wu, F.; Hu, Y.; Sheng, Z.; Wang, M.; Zhang, M.; Wang, S.; Chen, X.; Hou, X. Controllable Liquid-Liquid Printing with Defect-Free, Corrosion-Resistance, Unrestricted Wetting Condition. *Iscience* **2019**, *19*, 93−100.

(7) Ming, C.; Yang, T.; Luan, K.; Chen, L.; Wang, L.; Zeng, J.; Li, Y.; Zhang, W.; Chen, L.-Q. Microstructural Effects on Effective Piezoelectric Responses of Textured Pmn-Pt Ceramics. *Acta Mater.* **2018**, *145*, 62−70.

(8) Hou, X.; Siwy, Z. S.; Ulbricht, M. *Advances in Multi-Scale Pores and Channels Systems*; Wiley, 2018.

(9) Hou, X. Smart Gating Multi-Scale Pore/Channel-Based Membranes. *Adv. Mater.* **2016**, *28* (33), 7049−7064.

(10) Nan, C. W.; Clarke, D. R. Piezoelectric Moduli of Piezoelectric Ceramics. *J. Am. Ceram. Soc.* **1996**, *79* (10), 2563−2566.

(11) Zheng, P.; Zhang, J. L.; Tan, Y. Q.; Wang, C. L. Grain-Size Effects on Dielectric and Piezoelectric Properties of Poled Batio3 Ceramics. *Acta Mater.* **2012**, *60* (13−14), 5022−5030.

(12) Niezgoda, S. R.; Yabansu, Y. C.; Kalidindi, S. R. Understanding and Visualizing Microstructure and Microstructure Variance as a Stochastic Process. *Acta Mater.* **2011**, *59* (16), 6387−6400.

(13) Lee, S. B.; Key, T. S.; Liang, Z.; García, R. E.; Wang, S.; Tricoche, X.; Rohrer, G. S.; Saito, Y.; Ito, C.; Tani, T. Microstructure Design of Lead-Free Piezoelectric Ceramics. *J. Eur. Ceram. Soc.* **2013**, *33* (2), 313−326.

(14) Garcia, R. E.; Craig Carter, W.; Langer, S. A. The Effect of Texture and Microstructure on the Macroscopic Properties of Polycrystalline Piezoelectrics: Application to Barium Titanate and Pzn-Pt. *J. Am. Ceram. Soc.* **2005**, *88* (3), 750−757.

(15) Bowen, C. R.; Topolov, V. Y. Piezoelectric Sensitivity of Pbtio3-Based Ceramic/Polymer Composites with 0−3 and 3−3 Connectivity. *Acta Mater.* **2003**, *51* (17), 4965−4976.

(16) Bostanabad, R.; Bui, A. T.; Xie, W.; Apley, D. W.; Chen, W. Stochastic Microstructure Characterization and Reconstruction Via Supervised Learning. *Acta Mater.* **2016**, *103*, 89−102.

(17) Feng, J.; Teng, Q.; He, X.; Wu, X. Accelerating Multi-Point Statistics Reconstruction Method for Porous Media Via Deep Learning. *Acta Mater.* **2018**, *159*, 296−308.

(18) Yang, W.; Wang, Z.; Yenusah, C.; Liu, Y. An Integrated Model for Prediction of Process-Structure-Property Relationship for Additively Manufactured Al-10si-Mg Alloy, *SAE Tech. Pap. Ser.* **2020**, 0148−7191.

(19) Bostanabad, R.; Zhang, Y.; Li, X.; Kearney, T.; Brinson, L. C.; Apley, D. W.; Liu, W. K.; Chen, W. Computational Microstructure Characterization and Reconstruction: Review of the State-of-the-Art Techniques. *Prog. Mater. Sci.* **2018**, *95*, 1−41.

(20) Srolovitz, D.; Anderson, M.; Grest, G.; Sahni, P. Computer Simulation of Grain Growth—I. Kinetics. *Acta Metall.* **1984**, *32*, 783.

(21) Wejchert, J.; Weaire, D.; Kermode, J. Monte Carlo Simulation of the Evolution of a Two-Dimensional Soap Froth. *Philos. Mag. B* **1986**, *53* (1), 15−24.

(22) Frost, H.; Thompson, C.; Howe, C.; Whang, J. A Two-Dimensional Computer Simulation of Capillarity-Driven Grain Growth: Preliminary Results. *Scr. Metall.* **1988**, *22* (1), 65−70.

(23) Soares, A.; Ferro, A.; Fortes, M. Computer Simulation of Grain Growth in a Bidimensional Polycrystal. *Scr. Metall.* **1985**, *19* (12), 1491−1496.

(24) Tanemura, M.; Ogawa, T.; Ogita, N. A New Algorithm for Three-Dimensional Voronoi Tessellation. *J. Comput. Phys.* **1983**, *51* (2), 191−207.

(25) Marsh, S.; Masumura, R.; Pande, C. A Curvature-Driven Vertex Model for Two-Dimensional Grain Growth. *Philos. Mag. Lett.* **1995**, *72* (6), 429−434.

(26) Hu, J. M.; Wang, B.; Ji, Y.; Yang, T.; Cheng, X.; Wang, Y.; Chen, L. Q. Phase-Field Based Multiscale Modeling of Heterogeneous Solid Electrolytes: Applications to Nanoporous Li3ps4. *ACS Appl. Mater. Interfaces* **2017**, *9* (38), 33341−33350.

(27) Tikare, V.; Holm, E.; Fan, D.; Chen, L.-Q. Comparison of Phase-Field and Potts Models for Coarsening Processes. *Acta Mater.* **1998**, *47* (1), 363−371.

(28) Krill, C., III; Chen, L.-Q. Computer Simulation of 3-D Grain Growth Using a Phase-Field Model. *Acta Mater.* **2002**, *50* (12), 3059−3075.

(29) Zeiler, M. D.; Fergus, R. Visualizing and Understanding Convolutional Networks. In *European Conference on Computer Vision*; Springer, 2014: pp 818−833.

(30) Albawi, S.; Mohammed, T. A.; Al-Zawi, S. Understanding of a Convolutional Neural Network. In *2017 International Conference on Engineering and Technology (ICET)*; IEEE: Piscataway, NJ, 2017; pp 1−6.

(31) Agrawal, A.; Choudhary, A. Deep Materials Informatics: Applications of Deep Learning in Materials Science. *MRS Commun.* **2019**, *9* (3), 779−792.

(32) Mani, M. P.; Aggarwal, H. K.; Ghosh, S.; Jacob, M. Model-Based Deep Learning for Reconstruction of Joint Kq under-Sampled High Resolution Diffusion MRI. In *2020 IEEE 17th International Symposium on Biomedical Imaging (ISBI)*; IEEE: Piscataway, NJ, 2020: pp 913−916.

(33) Sundararaghavan, V.; Zabaras, N. Classification and Reconstruction of Three-Dimensional Microstructures Using Support Vector Machines. *Comput. Mater. Sci.* **2005**, *32* (2), 223−239.

(34) Mosser, L.; Dubrule, O.; Blunt, M. J. Stochastic Reconstruction of an Oolitic Limestone by Generative Adversarial Networks. *Transp. Porous Media* **2018**, *125* (1), 81−103.

https://doi.org/10.1021/acsami.1c12945
ACS Appl. Mater. Interfaces 2021, 13, 53439−53453

(35) Li, X.; Zhang, Y.; Zhao, H.; Burkhart, C.; Brinson, L. C.; Chen, W. A Transfer Learning Approach for Microstructure Reconstruction and Structure-Property Predictions. *Sci. Rep.* **2018**, *8* (1), 13461.
(36) Cang, R.; Xu, Y.; Chen, S.; Liu, Y.; Jiao, Y.; Yi Ren, M. Microstructure Representation and Reconstruction of Heterogeneous Materials Via Deep Belief Network for Computational Material Design. *Journal of Mechanical Design* **2017**, *139*, 7.
(37) Goodfellow, I.; Pouget-Abadie, J.; Mirza, M.; Xu, B.; Warde-Farley, D.; Ozair, S.; Courville, A.; Bengio, Y. Generative Adversarial Nets. *Commun. ACM* **2014**, *63*, 2672−2680.
(38) Mirza, M.; Osindero, S. Conditional Generative Adversarial Nets. *arXiv preprint* **2014**, arXiv:1411.1784.
(39) Isola, P.; Zhu, J.-Y.; Zhou, T.; Efros, A. A. Image-to-Image Translation with Conditional Adversarial Networks. *In Proceedings of the IEEE conference on computer vision and pattern recognition* **2017**, 1125−1134.
(40) Zhang, H.; Xu, T.; Li, H.; Zhang, S.; Wang, X.; Huang, X.; Metaxas, D. N. Stackgan++: Realistic Image Synthesis with Stacked Generative Adversarial Networks. *IEEE transactions on pattern analysis and machine intelligence* **2019**, *41* (8), 1947−1962.
(41) Ma, B.; Wei, X.; Liu, C.; Ban, X.; Huang, H.; Wang, H.; Xue, W.; Wu, S.; Gao, M.; Shen, Q.; Mukeshimana, M.; Abuassba, A. O.; Shen, H.; Su, Y. Data Augmentation in Microscopic Images for Material Data Mining. *npj Computational Materials* **2020**, *6*, 1.
(42) Chun, S.; Roy, S.; Nguyen, Y. T.; Choi, J. B.; Udaykumar, H. S.; Baek, S. S. Deep Learning for Synthetic Microstructure Generation in a Materials-by-Design Framework for Heterogeneous Energetic Materials. *Sci. Rep.* **2020**, *10* (1), 13307.
(43) Gayon-Lombardo, A.; Mosser, L.; Brandon, N. P.; Cooper, S. J. Stochastic Reconstruction of Periodic, Three-Dimensional Multi-Phase Electrode Microstructures Using Generative Adversarial Networks. *arXiv preprint* **2020**, arXiv:2003.11632.
(44) Naeini, K. N. *Structure Guided Image Restoration: A Deep Learning Approach,*; University of Ontario Institute of Technology: Oshawa, Ontario, Canada, 2019.
(45) Zhang, H.; Xu, T.; Li, H.; Zhang, S.; Wang, X.; Huang, X.; Metaxas, D. N. Stackgan: Text to Photo-Realistic Image Synthesis with Stacked Generative Adversarial Networks. *In Proceedings of the IEEE international conference on computer vision* **2017**, 5907−5915.
(46) Singh, R.; Shah, V.; Pokuri, B.; Sarkar, S.; Ganapathysubramanian, B.; Hegde, C. Physics-Aware Deep Generative Models for Creating Synthetic Microstructures. *arXiv preprint* **2018**, arXiv:1811.09669.
(47) Li, X.; Yang, Z.; Brinson, L. C.; Choudhary, A.; Agrawal, A.; Chen, W. A Deep Adversarial Learning Methodology for Designing Microstructural Material Systems. In *International Design Engineering Technical Conferences and Computers and Information in Engineering Conference*; American Society of Mechanical Engineers: New York, 2018; Vol. *51760*, p V02BT03A008.
(48) Igathinathane, C.; Pordesimo, L.; Columbus, E.; Batchelor, W.; Methuku, S. Shape Identification and Particles Size Distribution from Basic Shape Parameters Using Imagej. *Computers and electronics in agriculture* **2008**, *63* (2), 168−182.
(49) Henriques, R.; Lelek, M.; Fornasiero, E. F.; Valtorta, F.; Zimmer, C.; Mhlanga, M. M. Quickpalm: 3d Real-Time Photo-activation Nanoscopy Image Processing in Imagej. *Nat. Methods* **2010**, *7* (5), 339.
(50) Schneider, C. A.; Rasband, W. S.; Eliceiri, K. W. Nih Image to Imagej: 25 Years of Image Analysis. *Nat. Methods* **2012**, *9* (7), 671.
(51) He, L.; Fei, F.; Wang, W.; Song, X. Support-Free Ceramic Stereolithography of Complex Overhanging Structures Based on an Elasto-Viscoplastic Suspension Feedstock. *ACS Appl. Mater. Interfaces* **2019**, *11* (20), 18849−18857.
(52) Fullwood, D. T.; Niezgoda, S. R.; Adams, B. L.; Kalidindi, S. R. Microstructure Sensitive Design for Performance Optimization. *Prog. Mater. Sci.* **2010**, *55* (6), 477−562.
(53) Hu, S.Y.; Chen, L.Q. A Phase-Field Model for Evolving Microstructures with Strong Elastic Inhomogeneity. *Acta Mater.* **2001**, *49*, 1879.
(54) Yu, P.; Hu, S. Y.; Chen, L. Q.; Du, Q. An Iterative-Perturbation Scheme for Treating Inhomogeneous Elasticity in Phase-Field Models. *J. Comput. Phys.* **2005**, *208* (1), 34−50.
(55) Kingma, D. P.; Ba, J. Adam: A Method for Stochastic Optimization. *arXiv preprint* **2014**, arXiv:1412.6980.
(56) Fokina, D.; Muravleva, E.; Ovchinnikov, G.; Oseledets, I. Microstructure Synthesis Using Style-Based Generative Adversarial Networks. *Phys. Rev. E: Stat. Phys., Plasmas, Fluids, Relat. Interdiscip. Top.* **2020**, *101* (4−1), 043308.
(57) Groeber, M. A.; Haley, B. K.; Uchic, M. D.; Dimiduk, D. M.; Ghosh, S. 3d Reconstruction and Characterization of Polycrystalline Microstructures Using a Fib−Sem System. *Mater. Charact.* **2006**, *57* (4−5), 259−273.
(58) Perkins, A.; Yang, W.; Liu, Y.; Chen, L.; Yenusah, C. Finite Element Analysis of the Effect of Porosity on the Plasticity and Damage Behavior of Mg Az31 and Al 6061 T651 Alloys In *ASME International Mechanical Engineering Congress and Exposition*; American Society of Mechanical Engineers: New York, 2019; Vol. *59469*, p V009T11A055.
(59) Brosnan, K. H.; Messing, G. L.; Meyer Jr, R. J.; Vaudin, M. D. Texture Measurements in < 001> Fiber-Oriented Pmn−Pt. *J. Am. Ceram. Soc.* **2006**, *89* (6), 1965−1971.
(60) Sabolsky, E.; James, A.; Kwon, S.; Trolier-McKinstry, S.; Messing, G. L. Piezoelectric Properties of < 001> Textured Pb (Mg 1/3 Nb 2/3) O 3−Pbtio 3 Ceramics. *Appl. Phys. Lett.* **2001**, *78* (17), 2551−2553.
(61) Tan, Y.; Zhang, J.; Wu, Y.; Wang, C.; Koval, V.; Shi, B.; Ye, H.; McKinnon, R.; Viola, G.; Yan, H. Unfolding Grain Size Effects in Barium Titanate Ferroelectric Ceramics. *Sci. Rep.* **2015**, *5* (1), 1−9.
(62) Radford, A.; Metz, L.; Chintala, S. Unsupervised Representation Learning with Deep Convolutional Generative Adversarial Networks. *arXiv preprint* **2015**, arXiv:1511.06434.
(63) Jung, J.; Yoon, J. I.; Park, H. K.; Jo, H.; Kim, H. S. Microstructure Design Using Machine Learning Generated Low Dimensional and Continuous Design Space. *Materialia* **2020**, *11*, 100690.
(64) Marselli, S.; Pavia, V.; Galassi, C.; Roncari, E.; Craciun, F.; Guidarelli, G. Porous Piezoelectric Ceramic Hydrophone. *J. Acoust. Soc. Am.* **1999**, *106* (2), 733−738.
(65) Ali, F.; Raza, W.; Li, X.; Gul, H.; Kim, K.-H. Piezoelectric Energy Harvesters for Biomedical Applications. *Nano Energy* **2019**, *57*, 879−902.
(66) Zheng, Q.; Shi, B.; Li, Z.; Wang, Z. L. Recent Progress on Piezoelectric and Triboelectric Energy Harvesters in Biomedical Systems. *Advanced Science* **2017**, *4* (7), 1700029.
(67) Dong, K.; Peng, X.; Wang, Z. L. Fiber/Fabric-Based Piezoelectric and Triboelectric Nanogenerators for Flexible/Stretchable and Wearable Electronics and Artificial Intelligence. *Adv. Mater.* **2020**, *32* (5), 1902549.
(68) González, J. L.; Rubio, A.; Moll, F. Human Powered Piezoelectric Batteries to Supply Power to Wearable Electronic Devices. *Int. J. Soc. Mater. Eng. Resour.* **2002**, *10* (1), 34−40.

https://doi.org/10.1021/acsami.1c12945
ACS Appl. Mater. Interfaces 2021, 13, 53439−53453